CHAPTER 1

INTRODUCTION

1.1 Background

Gas sensors are of great importance for many applications including industrial production, environmental monitoring, medical diagnosis, domestic security, etc. There are several gasses known to be harmful to humans and the environment and to protect people and the environment from these harmful gases affordable gas sensors with higher detecting capacity and gas selectivity are needed. Such devices are suitable to detect the presence of low concentration target gasses and give warnings or send message for proper action when the designed threshold value is attained. For example health related problems may result from low indoor air quality due to various pollutants and immediate ventilation of these species is desirable when the limit is reached [1].

Semiconducting metal oxide sensors are one of the most widely studied due to their simple implementation, low cost and good reliability for real-time control systems [2−4]. Most of research in gas sensing devices has been focused on metal oxide materials such SnO_2, ZnO, TiO_2, α-Fe_2O_3, WO_3 and so on. These candidates have non-stoichiometric structures, so free electrons originating from oxygen vacancies contribute to electronic conductivity when the composition of the surrounding atmosphere is altered [5−11]. The gas sensing properties of these types of oxides are determined by their intrinsic properties, addition of impurities into the oxides and film microstructure including particle size, distribution and and orientation surface morphology and porosity [1].

Tungsten trioxide (WO_3) is one of promising materials for semiconductor gas sensors. WO_3 can operate at elevated temperatures for long periods of time and can detect NO_x, H_2S, C_2H_5OH, CO and NH_3 even in the presence of other gases such as CH_4 and H_2. It is well known that WO_3 like the majority of metal oxide-based gas sensors suffer from drift and lack of selectivity, and in order to solved these problems, a number of different strategies were applied such as the sensor's dynamic response analysis as well as mixed oxides sensors for gas detection [12].

In addition to the previous cited strategies, the modification of the metal oxide active layer by adding small amount of noble metals has been recently emerged as a promising way for the improvement of sensors. Catalysts like Au, Pd and Pt are often added [13−15] to the base material to improve the gas sensitivity and selectivity. Among various additives tested, Platinum (Pt) is known to be the most effective catalyst that can greatly promote sensing of reducing gas including hydrogen, carbon monoxide and hydrocarbon by chemical sensitization via 'spillover' effect [16, 17]. It can be effectively used to increase response and selectivity as well as to reduce response and recovery times.

Flame spray pyrolysis (FSP) is a relatively new synthesis method that has not yet been extensively studied for sensor fabrication. FSP is a versatile technique that can produce high purity nano-sized materials with well-controlled size and crystallinity. Therefore, FSP should be very promising technique for sensor material fabrication since it enables excellent control of specific surface area. In FSP method, specific surface area can be increased by increasing an oxidant flow rate and reducing spray flame length, which lead to shorter residence times for particle grow [18, 19]. FSP has another key advantage of allowing one to completely manufacture the nanopowder in a single high-temperature step without affecting the microstructure and particle size in a subsequent annealing process. Moreover, loading or doping with metals or other metal oxides can easily be done by FSP technique. And also wet chemical method offer significant advantages, such as total control over their shape and size, low processing temperature, high homogeneity, cost effectiveness, and easy synthesis [20].

In present study, a promoting way to prepare selective and sensitive gas sensor based on Pt–loaded WO_3 is presented, and the gas responses towards different oxidizing and reducing gases are comparatively investigated.

1.2 Tungsten trioxide (WO_3)

WO_3 is an n-type semiconductor with a band gap of about 2.6−2.8 eV [21]. The intrinsic conductivity arises from its non-stoichiometric composition giving rise to a donor level formed by oxygen vacancy defect in the lattice. Since the tungsten has many oxidation states, i.e., 2, 3, 4, 5 and 6, the tungsten compound can exist in many forms. For instance, the typical forms of tungsten oxides are tungsten (VI) oxide (WO_3, lemon yellow appearance) and tungsten (IV) oxide (WO_2, brown and blue appearance) [22]. Such electronic properties make the tungsten oxides suitable for various applications such as electrochromics, photochromics, photocatalysts, and gas sensors. A possibility of using nanostructured WO_3 as gas sensitive material has been widely studied in recent years since such particle possess large surface area for adsorption/desorption of gas molecules, and therefore is expected to enhance gas sensing performance [23]. Until now various methods for the synthesis of nanostructured WO_3 with various morphologies have been reported such as pyrolysis [24], thermal decomposition [25], and wet chemical process such as sol-gel [26], colloidal process [27], and solvothermal/hydrothermal method [28−31].

WO_3 exhibits a cubic perovskite-like structure based on the corner sharing of WO_6 regular octahedral, with the O atoms (W atoms) at the corner (centre) of each octahedron [33] (Figure 1.1). The crystal network can also be viewed as the results of alternating disposition of O and WO_2 planes, placed normally to each main crystallographic direction. This structure is also found in rhenium trioxide structure (ReO_3), from which takes its common name (ReO_3-structure). This structure is in itself rather uncommon. However, since it forms the base of perovskites (one of the most important ternaries), it has in fact chief importance.

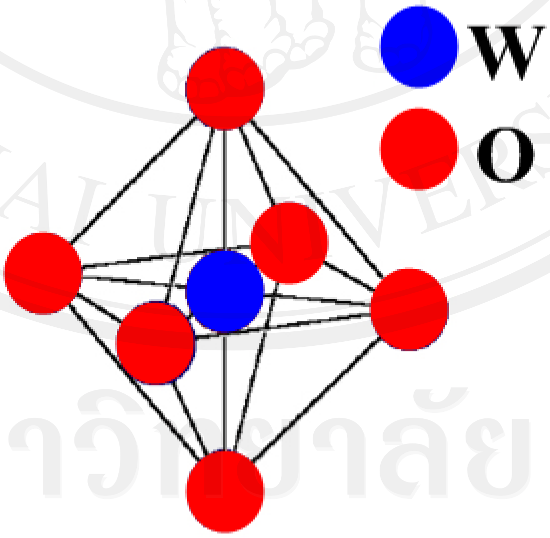

Figure 1.1 Schematic model of crystalline WO_3 in the undistorted cubic phase. The unit octahedron presents the tungsten atom at the centre and 6 equivalent oxygen atoms at the corners.

Actually, the symmetry of tungsten oxide is lowered from the ideal ReO_3 structure by two distortions: tilting of WO_6 octahedra and displacement of tungsten from the centre of its octahedron [33]. Variations in the details of these distortions give rise to several phase transitions. In fact tungsten trioxide adopts at least five distinct crystallographic modifications between absolute zero and its melting point at 1427°C. When the temperature is decreased from the melting point, the crystallographic symmetry for WO_3 changes in the sequence: tetragonal-orthorhombic-monoclinic-triclinic-monoclinic. Most of the transitions appear to be first order, and they often display large hysteresis in the transition temperatures. A summary of these transitions is given in Table 1.1.

Table 1.1 Known polymorphs of tungsten trioxide [34−40].

Phase	Symmetry	Point group	Temperature range (°C)
α-WO_3	Tetragonal	P4/nmm	> 720
β-WO_3	Orthorhombic	Pmnb	320−720
γ-WO_3	Monoclinic	$P2_1/n$	17−320
δ-WO_3	Triclinic	P1	– 40−17°C
ε-WO_3	Monoclinic	Pc	< − 40°C

It is interesting to notice that, as suggested by Table 1.1 and was confirmed experimentally in [41], the coexistence of triclinic and monoclinic phase in WO_3 at room temperature is common.

The chemical and physical properties of WO_3 are shown in Table1.2. To realize any type of device technology, it is important to have control over the concentration of intentionally introduced impurities, called dopants, which are responsible for the electrical properties of WO_3. The dopants determine whether the current (and, ultimately, the information processed by the device) is carried by electrons or holes.

Table 1.2 Properties of WO_3 [21, 42].

Property	Value
Molar mass	231.84 $g \cdot mol^{-1}$
Appearance	Yellow powder
Density	7.16 $g \cdot cm^{-3}$
Melting point	1473^{o}C
Boiling point	~1700^{o}C
Energy gap	2.6-2.8 eV
Solubility in water	Insoluble

1.3 Platinum (Pt) [43]

Platinum is a chemical element with the chemical symbol Pt and an atomic number of 78. Its name is derived from the Spanish term platina del Pinto, which is literally translated into "little silver of the Pinto River." It is in Group 10 of the periodic table of elements. A dense, adaptable, ductile, precious, gray-white transition metal, platinum is resistant to corrosion and occurs in some nickel and copper ores along with some native deposits. Platinum is used in jewelry, laboratory equipment, electrical contacts and electrodes, platinum resistance thermometers, dentistry equipment, and catalytic converters. Platinum's most common oxidation states are +2, and +4. The +1 and +3 oxidation states are less common, and are often stabilized by metal bonding in bimetallic (or polymetallic) species. As is expected, tetracoordinate platinum(II) compounds tend to adopt a square planar geometry. While elemental platinum is generally unreactive, it dissolves in aqua regia to give soluble hexachloroplatinic acid.

The most common use of platinum is as a catalyst in chemical reactions. It has been employed in this application since the early 1800s, when platinum powder was used to catalyze the ignition of hydrogen. The most important application of platinum is in automobiles as a catalytic converter, which allows the complete combustion of low concentrations of unburned hydrocarbon from the exhaust into carbon dioxide and water vapor. Platinum is also used in the petroleum industry as a catalyst in a number of separate processes, but especially in catalytic reforming of straight run naphthas into higher-octane gasoline which becomes rich in aromatic compounds. PtO_2, also known as Adams' catalyst, is used as a hydrogenation catalyst, specifically for vegetable oils. Platinum metal also strongly catalyzes the decomposition of hydrogen peroxide into water and oxygen gas. The chemical and physical properties of platinum are shown in Table1.3

Table 1.3 Chemical and physical properties of Pt [43].

Property	**Value**
Stand atomic weight	195.084
Phase	Solid
Density	21.45 $g \cdot cm^{-3}$
Melting point	1768^{o}C
Boiling point	3825^{o}C
Heat of fusion	22.17 $kJ \cdot mol^{-1}$
Heat of vaporization	469 $kJ \cdot mol^{-1}$
Molar heat capacity	25.86 $J \cdot mol^{-1} \cdot K^{-1}$
Crystal structure	Face-centered cubic
Electrical resistivity	(20^{o}C) 105 $n\Omega \cdot m$
Thermal conductivity	71.6 $W \cdot m^{-1} \cdot K^{-1}$

1.4 Powder preparation

1.4.1 Thermal decomposition method [44, 45]

Thermal decomposition is defined as a chemical reaction whereby a chemical substance breaks up into at least two chemical substances when heated. It is usually an endothermic reaction as heat is required to break chemical bonds in the compound undergoing decomposition. *Thermolysis* (from *thermo*- meaning heat and -lysis meaning break down) is a chemical process by which a substance is decomposed into other substances by use of heat. The decomposition temperature of a substance is the temperature at which the substance decomposes into smaller substances or into its constituent atoms. High temperatures can also induce polymerization, which produces larger molecules, possibly also causing thermal decomposition and evaporation of smaller molecules in the process.

1.4.2 Sol-gel method [46−48]

The sol-gel process allows synthesizing ceramic materials of high purity and homogeneity by mean of preparation techniques different from the traditional process of fusion of oxides. This process occurs in liquid solution of organometallic precursors which, by means of hydrolysis and condensation reactions, lead to the formation of a new phase (sol). The reaction schemes were described by reaction (1.1)-(1.3)

$$\text{M-O-R} + H_2O \rightarrow \text{M-OH} + \text{R-OH (hydrolysis)} \qquad (1.1)$$

$$\text{M-OH} + \text{HO-M} \rightarrow \text{M-O-M} + H_2O \text{ (water condensation)} \qquad (1.2)$$

$$\text{M-O-R} + \text{HO-M} \rightarrow \text{M-O-M} + \text{R-OH (alcohol condensation)} \qquad (1.3)$$

The sol is made of solid particles of diameter of few hundreds nm suspended in a liquid phase. Then the particles condense in a new phase (gel) in which a solid macromolecule is immersed in a liquid phase (solvent). Drying the gel by means of low temperature treatments (25−100^{o}C), it is possible to obtain porous solid matrices.

The sol-gel process can be divided into six steps as depicted schematically in Figure 1.2.

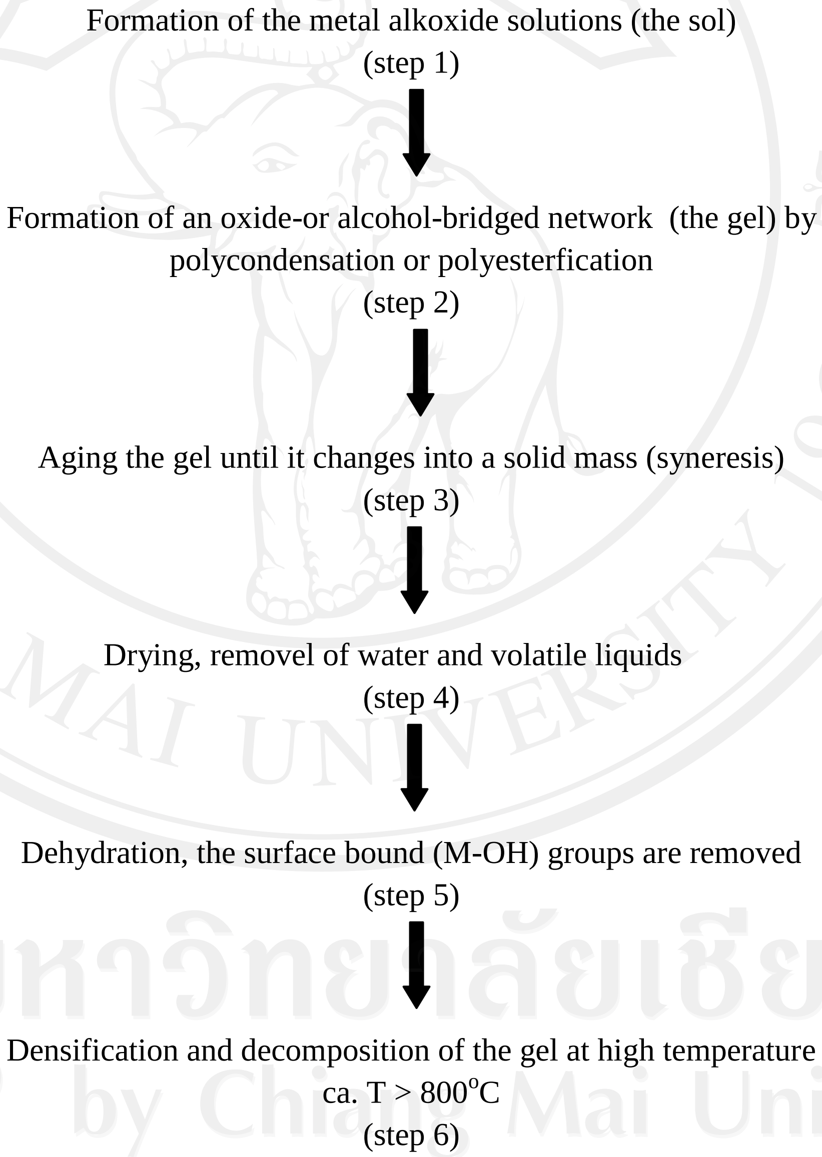

Figure 1.2 Typical steps for sol-gel process

The fundamental property of the sol-gel process is that it is possible to generate ceramic material at a temperature close to room temperature. Therefore such a procedure opened the possibility of incorporating in these glasses soft dopants, such as fluorescent dye molecules and organic chromophores into ceramic substrates.

1.4.3 Microemulsion method [49−51]

Microemulsions are formed when a combination of water, oil, surfactant and co-surfactant are stirred together. The micelle cores created act as a template for particles to grow, therefore controlling the size of the synthesized particles. The size of these cores is dependent on the molar ratio of water to surfactant, *w*. This thus creates a means to control particle size. This is illustrated by the Schulman's model for the water-in-oil micelle as in Figure 1.3. The radius, r_2 for the outer shield is surrounded by the surfactants and co-surfactants. They provide a barrier to prevent aggregation between the particles. As for the size of the particles they are restricted by radius, r_1 where the prepared particles will have a diameter that is less than $2r_2$.

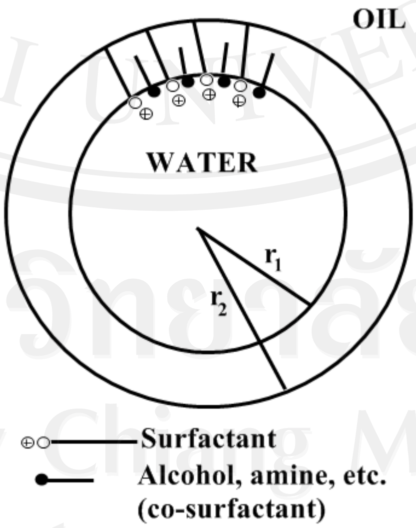

Figure 1.3 Schulman's model for the reverse micelle

1.4.4 Sonochemical reduction method [52−54]

Sonochemical reduction is one of the earliest techniques used to prepare nanoparticles. It involves ultrasound irradiation (frequency range 20kHz-10 MHz) that can break the chemical bonding of the precursors. The chemical effects of the ultrasound arise from acoustic cavitation–formation, growth, and implosive collapse of bubbles in liquids. There are two regions of sonochemical reactivity, the inside zone of the collapsing bubble and the interface between bubbles and the liquid. The cavitation may generate very high temperature over 5000 K and pressure over 20MPa, which enable many chemical reactions to occur. In short, during the process, the implosive collapse of bubbles generates localized hot spots through adiabatic compression or shockwave formation within the gas phase of the collapsing bubbles. These extreme conditions attained during bubble collapse have been exploited to prepare various materials with different morphologies [53, 54]

1.4.5 Precipitation method [50, 55]

Essentially, the preparation of metal oxides can be divided into two types: i.e. either the generation of the metal oxide direction or production of appropriate intermediates which require further processing (such as calcinations and drying). This latter method involves suitable metal salts oxidation in aqueous or non-aqueous medium using precipitating agents. Occasionally, high temperatures are required to produce crystalline products.

1.4.6 Hydrothermal method [56−58]

The original hydrothermal method involves heating the reaction in a closed vessel (an autoclave) with water. In a closed vessel the pressure increases and the water remains liquid above its normal boiling temperature of 100°C. These conditions, in which the temperature is raised above boiling temperature of water and the pressure raised above atmospheric pressure, are known as hydrothermal conditions. Powders prepared via hydrothermal method are often unagglomerated, anhydrous and crystalline. Consequently, the prepared powders do not have to be calcined or milled. They remain unagglomerated and substantially free of impurities.

Hydrothermal synthesis offers a potentially superior technique for low cost and low temperature production of piezoelectric materials. Normally, hydrothermal synthesis has been used for preparing ceramic powders for a variety of applications. It has superiority over the other powder preparation methods in that high calcinations temperature is not necessary for the synthesis of crystallized ceramic powders.

1.4.7 Impregnation method [59, 60]

Impregnation method is considered as a simple method of making a catalyst. The powder of catalyst is contacted with a solution then dried and calcined. The impregnation technique requires less equipment since the filtering and forming steps are eliminated and washing may not require. It is a preferred method in preparing metal ions coating on surface of semiconductors such as TiO_2, ZnO, SnO_2 and WO_3 due to its simplicity.

1.4.8 Flame spray pyrolysis [60−70]

Flame aerosol technology is the important key process for large-scale production of nano-structured materials such as carbon blacks, fumed SiO_2 and TiO_2 and to a lesser extent, for specialty chemicals such as Al_2O_3 and ZnO powders. Flame aerosol synthesis is a cost-effective and versatile process for controlled production of nanoparticles [60−63]. Flame spray pyrolysis (FSP) process was systematically investigated using an external-mixing gas-assisted atomizer supported by premixed methane and oxygen flamelets [64, 65]. In flame reactors, the energy of flame is used to drive chemical reactions of precursors resulting in clusters which further grow to nanoparticles by surface growth and/or coagulation and coalescence at high temperature. The advantage of FSP include the ability to dissolve the precursor directly in the fuel, simplicity of introduction of the precursor into the hot reaction zone (e.g. a flame), and flexibility in using the high-velocity spray jet for rapid quenching of aerosol formation. In general, a flame is used to force chemical reactions of precursor compounds, finally resulting in the formation of clusters, which increase their size to a range of some nanometers by coagulation and sintering. Finally, the nanostructured powders are collected on a filter [64, 65]. The more fuel introduced the higher the flame is and due to the resident time of particles in the flame is also increased. As a consequence time for particle growth is prolonged the bigger particles are formed. External electric field reduces the average particle size in a narrow range up to a factor of two. Electric fields can be used in application as control devices [66, 67]. The basic mechanism for formation of supported platinum group metal (pgm) particles was shown in Figure 1.4.

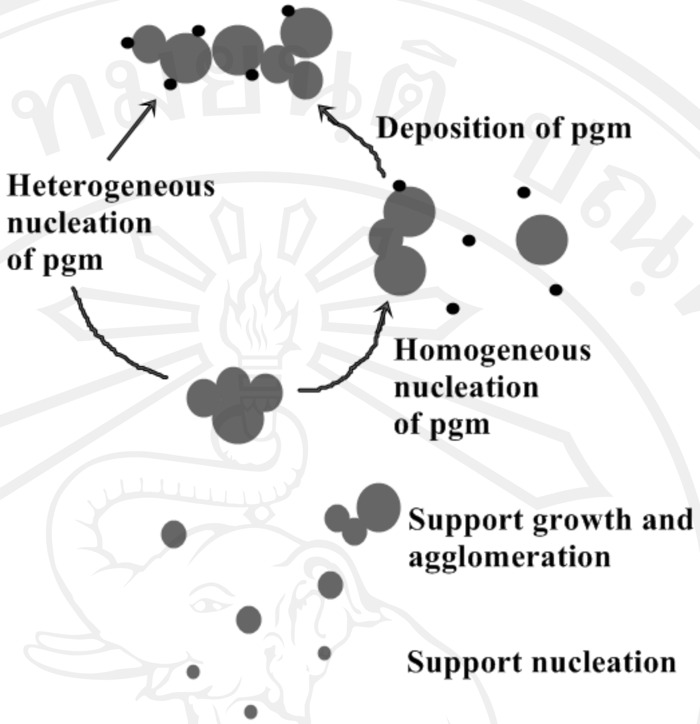

Figure 1.4 Schematic for the formation of supported metals in a flame. In a first step the support is formed by nucleation from the gas phase, and then at lower temperatures pgms nucleate heterogeneously on the support and/or homogeneously from the gas with deposition on the support [68].

Moreover, at low oxidant flow rates, the specific surface area increased with increasing oxidant flow rate as the spray flame length was reduced, leading to shorter resident time and allowing less time for particle growth. Using pure oxygen as oxidant the droplets burn much faster than with air, thus, product particles experience longer resident times at higher temperature [63−70]. The effect of solution feed rate on particles specific surface area and crystalline size was also investigated [62]. The solution feed rate increased the flame height, and therefore coalescence was enhanced, resulting in large primary particles [62].

1.5 Characterization techniques

1.5.1 X-ray diffraction method [71−76]

X-ray diffraction (XRD) is a standard tool for identification of crystalline phases in powder samples. The crystalline phase in the sample diffracts X-rays according to Bragg's equation which relates lattice spacing to the wavelength of the X-ray. The amount of sample needed in practice is roughly 100 mg or more. Crystalline phases present at the levels of about 1 percent or greater can be detected. The unit cell dimension (a,b,c) of the crystal can also be determined and provide more information for complex structure materials. Amorphous materials are not observed. In routine work, XRD relies on availability of standards that allow identification of peaks in the diffraction pattern.

1.5.1.1 The advantage of X-ray diffraction method

The simplicity and advantages of the powder diffraction method for identification of an unknown substance are as follows:

- The powder diffraction pattern is determined by the exact atomic arrangement in a material, so it is like a "fingerprint" of the material.
- Each substance in a mixture produces its own characteristic diffraction pattern independently of the others.
- The X-ray diffraction pattern discloses the presence of a substance as that substance actually exists in the specimen.
- Only a small amount of the material is required for recording the X-ray diffraction pattern.
- The method is nondestructive.

1.5.1.2 Identification of crystal structure by XRD

The X-ray diffraction pattern is a fingerprint of any substance, it should be possible to unambiguously identify that material from its X-ray diffraction pattern. A large collection of X-ray diffraction pattern from a number of substances are available, then the unknown material can be identified by obtaining its diffraction pattern and then determining which pattern from the collection matches exactly with the library diffraction pattern. The Powder Diffraction File (PDF) organized by the Joint Committee on Powder Diffraction Standards (JCPDS), later renamed the International Centre for Diffraction Data (ICDD), and at present collections of nearly 80,000 standard diffraction patterns.

1.5.1.3 Diffraction from Crystalline Materials-Bragg's Law

Bragg law, formulated by W.L. Bragg in 1913, relates the wavelength of the X-rays to the spacing of the atomic planes. Consider the diffracted wave in Figures 1.5 and 1.6. It is assumed to make the same angle, θ, with the atomic planes as does the incident wave. The criterion for the existence of the diffracted wave is that the scattered (reflected) X-ray should all be in phase across a wavefront. This turns out to be a real convenience, so we set $d = d'/n$ and write the Bragg law in the form

$$\lambda = 2d\sin\theta \qquad (1.4)$$

This equation is known as Bragg's law and is extremely important in indexing X-ray diffraction patterns and, hence, for determining things like the crystal structure of the material.

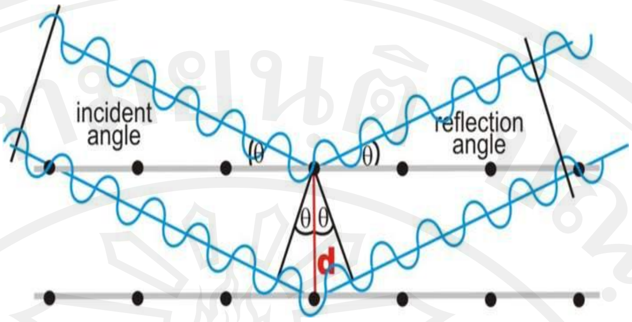

Figure 1.5 Diffraction of X-rays by a crystal. Destructive interference of reflected waves (in the reflected waves, maximum and minimum of the wave amplitude are superimposed) [73].

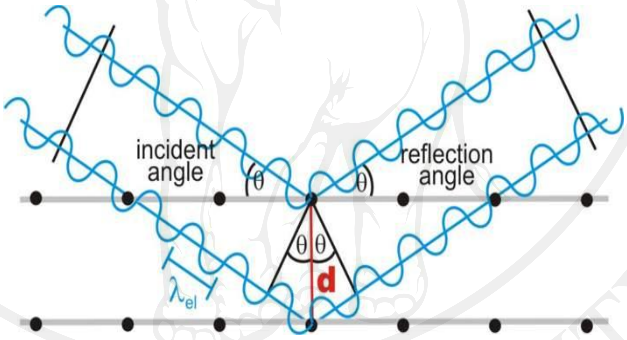

Figure 1.6 Constructive Interference of reflected waves (reflected waves in phase, i.e., maxima are superimposed) [73].

The scattering of electrons, X-rays and neutrons by crystals can be described as a reflection of the beams at planes of atoms (lattice planes), independent of the actual physical reason causing the diffraction event. If the incident plane wave hits the crystal at an arbitrary angle, the interference of the reflected waves can be either destructive or constructive. To obtain constructive interference, the path difference between the two incident and the scattered waves, which is 2dsinθ, has to be a multiple of the wavelength λ. For this case, the Bragg law then gives the relation between interplanar distance d and diffraction angle θ

1.5.1.4 Particle size measurement by XRD

For good quality crystalline material of dimension 0.1 nm is made up of approximately 1,000,000 crystal planes (assuming that d_{hkl} = 1 nm). When an X-ray collides with these planes close to the Bragg angle, diffraction intensity is not observed because the X-rays reflected from the multitude of parallel planes annihilate one another. With such materials diffraction peaks are produced only within a very narrow window very close to the Bragg angle. Particle sizes are often in the range 1−100 nm for heterogeneous catalysts. In such circumstances the number of stacked planes per particle is in the range of 5−100. This results in the broadening of the XRD peaks because there are insufficient reflecting planes to annihilate phase reflection at angle that are fairly far and removed from the Bragg angle.

This effect has been quantified as the Scherrer equation:

$$t_{\mathrm{hkl}} = K\lambda / B_{\mathrm{hkl}} \cos\theta_{\mathrm{hkl}} \qquad (1.5)$$

Where:

t_{hkl} is the particle size measured from X-rays diffracted from the (*hkl*) planes

B_{hkl} is the full-width at half-maximum (FWHM) of the peak measured in radian from the (*hkl*) planes

θ_{hkl} is the Bragg angle for the reflection from the (*hkl*) planes

K is a constant which depends to some extent on the particles shape. For spherical particles K = 0.9.

Figure 1.7 demonstrates how particle size and shape can be determined by XRD analysis. A sample was analyzed by XRD and exhibited the pattern shown, namely one very narrow line and another rather broad. In this case the apparent conflict is caused by the shape of particle. X-rays reflected from the (100) planes, a large particle and a narrow line results. X-rays reflected from the (001) planes, a small particle and a broad line results.

When measuring particles size using XRD line broadening it is important to realize that not all the broadening is due to the particle size effect. Near perfect crystals should produce extremely narrow XRD lines, but even here some broadening occurs because of instrumental factors. Instrumental contribution to line broadening should be subtracted out by running the XRD of a good quality polycrystalline sample versus the same materials.

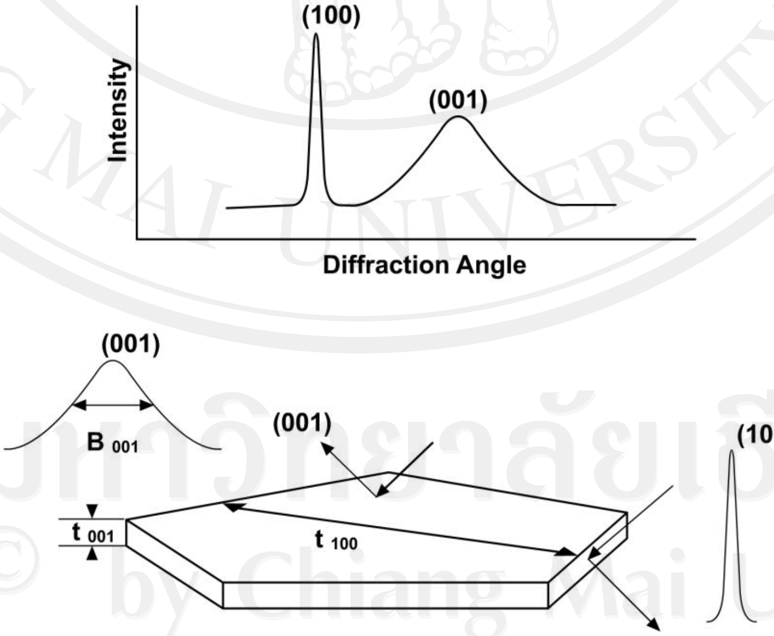

Figure 1.7 Schematic diagram of X-ray line broadening effects [76]

1.5.1.5 Sample preparation

In X-ray diffraction work, normally distinguishes between single crystal and polycrystalline or in powder applications. The single crystal sample is a perfect (all unit cells aligned in a perfect extended pattern) crystal with a cross section of about 0.3 mm. The single crystal diffractometer and associated computer package is used mainly to elucidate the molecular structure of novel compounds, either natural products or man-made molecules. Powder diffraction is mainly used for “finger print identification” of various solid materials, e.g. asbestos, quartz etc.

In powder or polycrystalline diffraction it is important to have a sample with a smooth plane surface. If possible, grinding the sample was normally performed down to particles of about 0.002 mm to 0.005 mm in cross section. The ideal sample is homogeneity and the crystallites are randomly distributed (problems which will occur if the specimen deviates from this ideal state will be pointed out later). The sample is pressed into a sample holder so that a smooth flat surface is obtained. Ideally, it should be a random distribution of all possible h, k, l planes. Only crystallites having reflecting planes (h, k, l) parallel to the specimen surface will contribute to the reflected intensities. In a truly random sample, each possible reflection from a given set of h, k, l planes will have an equal number of crystallites contributing to it. The sample needs to be fixed through the glancing angle θ in order to produce all possible reflections.

1.5.2 Scanning Electron Microscopy (SEM) [77−79]

1.5.2.1 Bulk specimen interactions

The energetic electrons in the microscopy strike the sample and various reactions can occur as shown in Figure 1.8a. The interactions sketched in the schematic drawing are utilized when examining thick or bulk specimens (SEM). A drawing showing the generation depths of the interactions is also presented in Figure 1.8b. In the SEM the following electrons are used for sample characterization:

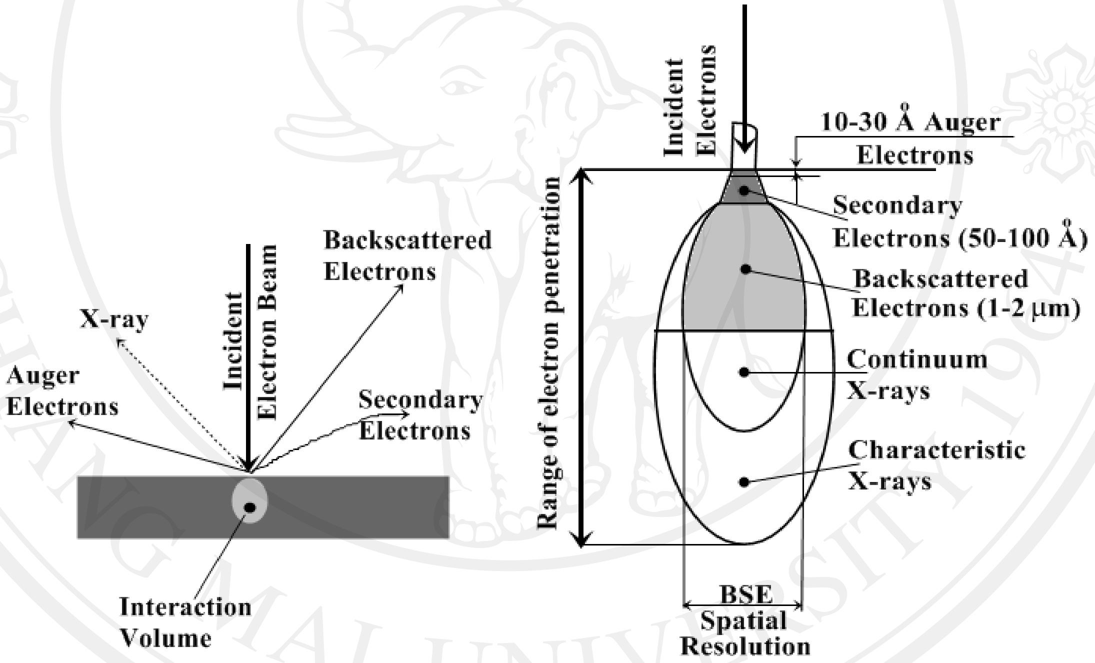

(a) The types of the interactions between a bulk specimen and the incident e-beam in a SEM.

(b) The interaction volume of the different electrons.

Figure 1.8 Interactions between the specimen and the electrons as well as penetration depths of different generated electrons in a bulk sample inside a SEM.

1.5.2.2 Secondary Electrons

They are caused by an incident electron passing “near” an atom in the specimen, near enough to impart some of its energy to a lower energy electron. This cause a slight energy loss and path change in the incident electron, a so called “secondary electron”, then leaves the atom with a very small kinetic energy.

1.5.2.3 Backscattered Electrons

They are caused by an incident electron colliding with an atom in the specimen which is nearly normal to the incident path. The incident electron is then scattered “backward” (180^{o}). The production of backscattered electrons varies directly with the spcimen’s atomic number. This differing generation rate causes higher atomic number elements to appear brighter than lower atomic number elements. This interaction is utilized to differentiate parts of the specimen that have different average atomic number.

1.5.2.4 Image formation inside a SEM

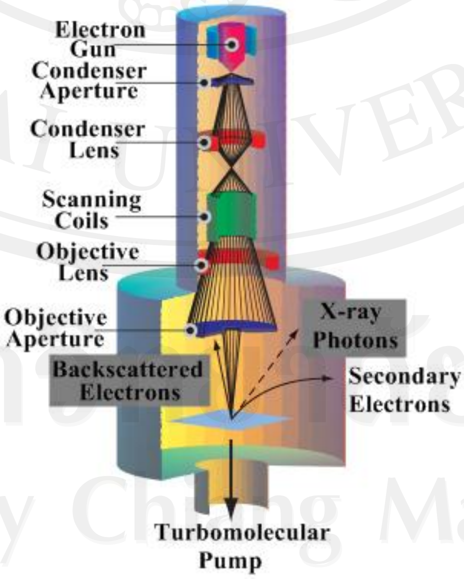

Figure 1.9 A schematic drawing of a SEM microscope including the interactions between a bulk specimen and the incident e-beam.

- At the top of the picture is an electron gun, producing a stream of monochoromatic electrons.
- The electron beam is condensed by the first condenser lens, which is used to form the beam. Together with the condenser aperture it eliminates the high-angle electrons from the beam.
- The second condenser lens forms the electrons into a thin, tight, coherent beam and is usually controlled by the “fine probe current”.
- A user selectable objective aperture further eliminates high-angle electrons from the beam.
- A set of coils then “scan” or sweep” the beam in a grid fashion like a television, dwelling on points for a period of time (usually in the microsecond range) determined by the scan speed.
- The final lens, the objective lens, focuses the scanning beam onto the desired part of the specimen.
- When the beam strikes the sample interactions occur inside the sample and are detected with various instruments.
- Before the beam moves to its next dwell point these detectors count the number of interactions and display a pixel on a screen whose intensity is determined by this number. Generally, the more reactions the brighter the pixel.
- This process is repeated until the grid scan is finished and then repeated.

1.5.3 Transmission Electron Microscopy (TEM) [79−82]

1.5.3.1 Thin specimen interactions

In a TEM, only thin specimens can be observed because electrons have a very short mean free path and can only be transmitted in a very thin sample. Thus, interactions between the specimen and the beam are different to those in a SEM. The interactions schematized in Figure 1.10 are those which take place in a TEM.

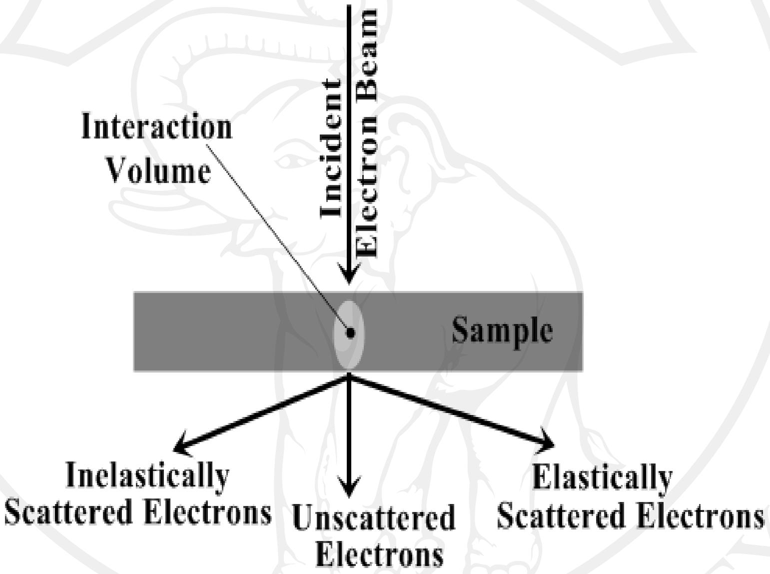

Figure 1.10 A schematic drawing of the interactions between an electron transparent specimen and the incident e-beam in a TEM.

1.5.3.2 Unscattered Electrons

Incident electrons are transmitted through the thin specimen without any interaction occurring inside the specimen. The transmission of unscattered electrons is inversely proportional to the specimen thickness. Areas of the specimen that are thicker will have less transmitted unscattered electrons and so will appear darker, conversely the thinner areas will have more transmitted and thus will appear brighter. The, so-called “bright-field” TEM images are composed of direct, unscattered electrons.

1.5.3.3 Inelastically Scattered Electrons

Incident electrons interacting with specimen atoms in an inelastic fashion, lose energy during the interaction. One use of the inelastically scattered electrons is for Electron Energy Loss Spectroscopy (EELS): The inelastic loss of energy by the incident electrons is characteristic of the elements that were interacted with. These energies are unique to each bonding state of each element and thus can be used to extract both compositional and bonding (i.e. oxidation state) information on the specimen region being examined.

1.5.3.4 X-rays

X-rays are caused by the de-energization of the specimen atom after a secondary electron is produced. Since a lower (usually K-shell) electron was emitted from the atom during the secondary electron process an inner (lower energy) shell now has a vacancy. A higher energy electron can “fall” into the lower energy shell, filling the vacancy. As the electron “falls” it emits energy, usually X-rays, to balance the total energy of the atom. X-rays emitted from the atom will have a characteristic energy which is unique to the element from which it originated. These signals are collected and sorted according to energy.

1.5.3.5 Image formation inside a TEM

The first TEM was developed by Max Knoll and Ernst Ruska in Germany in 1931. A TEM works much like a slide projector, which shines a beam of light through the slide. As the light passes through it is affected by the structures and objects on the slide. These effects result in only certain parts of the light beam being transmitted through certain parts of the slide. This transmitted beam is then projected onto the viewing screen, forming an enlarged image of the slide.

In the TEM, the sample is illuminated with an electron beam using condenser lenses. The resulting image, representing a 2D projection of the sample, is magnified by the projector lens before being collected on a fluorescent screen, photographic paper or a CCD camera. The main limiting factor in TEM resolution is not the electron wavelength but the aberrations due to electromagnetic lenses that result in a 1 Å resolution for state-of-the-art microscopes.

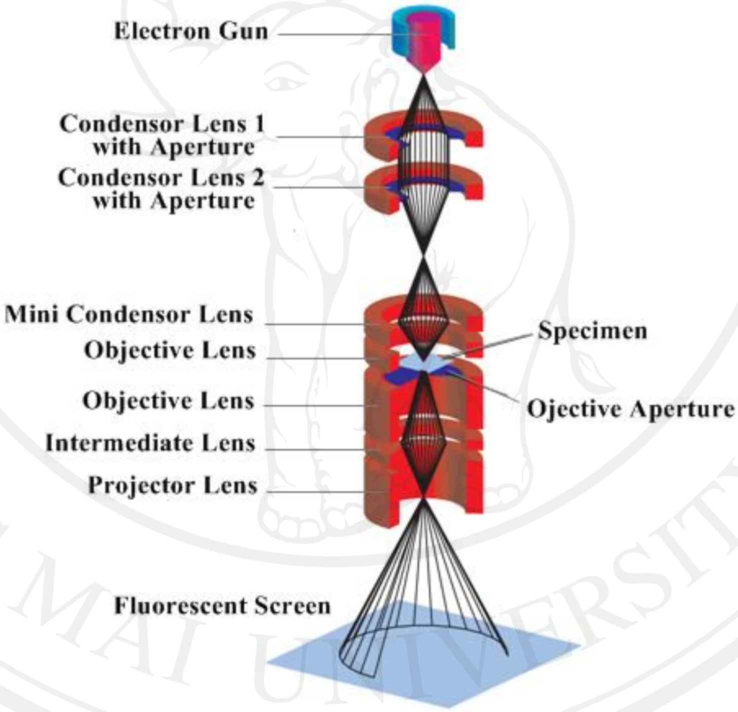

Figure 1.11 A simplified schematic drawing of the main components of a transmission electron microscope.

- The electron gun, produces a coherent monochromatic electron beam, as in the case of SEM.
- This beam is focused by the use of condenser lenses 1 and 2. The first lens largely determines the “spot size”; the general size range of the final spot that strikes the sample. The second lens changes the size of the spot on the sample; changing it from a wide dispersed spot to a pinpoint beam.
- The beam is restricted by the condenser aperture, to filter high angel electrons.
- The beam strikes the specimen and parts of it are transmitted.
- The objective lens is the most critical lens since it determines the resolving power of the instrument and performs the first stage of imaging. The objective aperture is positioned in the back focal plane of the objective lens, where electron diffraction patterns are formed, and limits the electron beams contributing to the final image. The selected area electron diffraction aperture can select the area of interest in order to obtain the diffraction pattern of that region.
- The image is passed down the column through the intermediate and projector lenses, being enlarged all the way.
- The image strikes the phosphor image screen and light is generated, allowing the user to see the image. The darker areas of the image represent those areas of the sample through which fewer electrons were transmitted (thicker or denser part of the sample).

1.5.4 The Brunauer-Emmett-Teller (BET) [83, 84]

BET theory is a well-known rule for the physical adsorption of gas molecules on a solid surface. In 1938, Stephen Brunauer, Paul Hugh Emmett, and Edward Teller published an article about the BET theory in a journal for the first time; “BET” consists of the first initials of their family names.

1.5.4.1 BET theory

The Brunauer-Emmett-Teller method is base on non-specific physisorption of a gas (N_2 or Ar) onto a solid close to the condensation temperature of the adsorbing gas. Adsorption is characterized by an isotherm which represents the equilibrium amount of gas adsorbed on a solid at a given temperature as a function of pressure.

The concept of the theory is an extension of the Langmuir theory, which is a theory for monolayer molecular adsorption, to multilayer adsorption with the following hypotheses:

(a) gas molecules physically adsorb on a solid in layers infinitely

(b) there is no interaction between each adsorption layer

(c) the Langmuir theory can be applied to each layer.

The resulting BET equation is expressed by (1.6):

$$\frac{1}{V\,[(Po/P)-1]} = \frac{1}{V_m C} + \frac{C-1}{V_m C}\,\frac{P}{Po} \qquad (1.6)$$

Where:

P and P_0 are the equilibrium and the saturation pressure of adsorbates at the temperature of adsorption,

V is the adsorbed gas quantity (for example, in volume units)

V_m is the monolayer adsorbed gas quantity

C is the BET constant, which is expressed by (1.7):

$$C = \exp\left(\frac{E_1 - E_L}{RT}\right) \quad (1.7)$$

Where:

E_1 is the heat of adsorption for the first layer

E_L is that for the second and higher layers and is equal to the heat of liquefaction.

1.5.4.2 BET plot

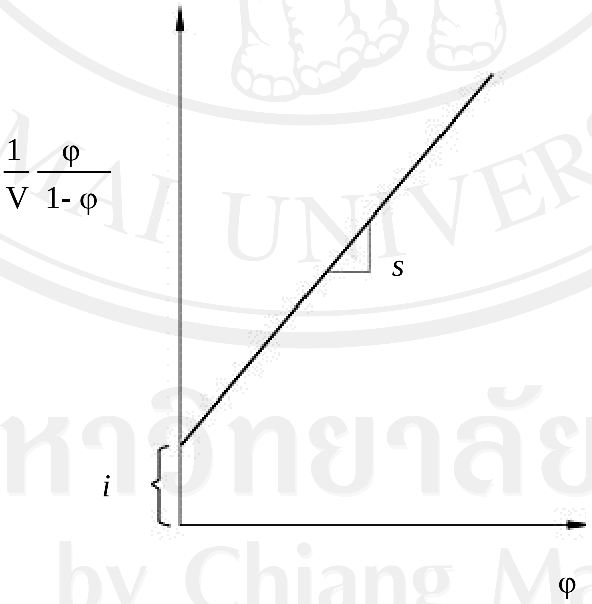

Figure 1.12 Typical BET plot [83]

Equation (1.6) is an adsorption isotherm and can be plotted as a straight line with $1 / V[(P_0 / P) - 1]$ on the y-axis and $\varphi = P / P_0$ on the x-axis according to experimental results. This plot is called a BET plot. The linear relationship of this equation is maintained only in the range of $0.05 < P / P_0 < 0.35$. The value of the slope s and the y-intercept i of the line are used to calculate the monolayer adsorbed gas quantity V_m and the BET constant C. The following equations can be used:

$$s = \frac{C\text{-}1}{V_m C} \tag{1.8}$$

$$i = \frac{1}{V_m C} \tag{1.9}$$

Solving the preceding equations for V_m and C gives

$$V_m = \frac{1}{s + i} \tag{1.10}$$

and

$$C = \frac{s}{i} + 1 \tag{1.11}$$

1.5.4.3 Surface area calculation

The BET method is widely used in surface science for the calculation of surface areas of solids by physical adsorption of gas molecules. A total surface area S_{total} and a specific surface area S are evaluated by the following equations:

$$S_{total} = \frac{V_m \bar{N} \cdot \mathcal{A}}{\bar{M}} \qquad (1.12)$$

Where:

S_{total}	is sample surface area
$\mathcal{A}$	is the cross-sectional area
$\bar{M}$	is the molecular weight of an adsorbate molecule
$\bar{N}$	is the Avogadro’s number

1.5.4.4 Particle Size (d_{BET})

The particle size (d_{BET}) is calculated by BET measurement using specific surface area (SSA) and density of sample by assuming that the particles do have spherical shape. The following equation can be used:

$$d_{BET} = \frac{6}{SSA_{BET}\,\rho_{sample}} \qquad (1.13)$$

Where: ρ_{sample} is the density of sample

1.6 Sensing performance factors [85−87]

As a new technique is developed, one needs to establish fairly quickly the criteria by which its performance can be measured. These criteria have to be refined continuously as expectations are raised. This is especially true for a device containing biological materials.

A number of different factors will be referred to in this part that applies to both biosensors and chemical sensors. Unfortunately, different workers express these factors in different ways, and worse still, some do not give much data at all about their performance in published papers. Anyone developing a new sensor needs to have some idea of what performance requirements are likely to be needed for a particular application.

1.6.1 Selectivity [86, 87]

The selectivity can be defined as the ability of a sensor to respond primarily to only on species in the presence of other species. This is the most important characteristic of sensors; the ability to discriminate between different substances. Such behavior is principally a function of the selective component, although sometimes the operation of the transducer contributes to the selectivity. This factor is the essence of sensors. It is the rate to find a sensor which will respond to only one analyte, although some do exist. It is more usual to find a sensor that will respond mainly to one analyte, with a limited response to other similar analyte. Alternately, the response may be to a group of analytes of similar chemical structure, such as carbonyl compounds.

1.6.2 Sensitivity [85, 87]

This usually need to be sub-millimolar, but in special cases can go down to the femtomolar (10−15 M) range. With any analytical technique, it is important to know what concentration range is covered and from the calibration point of view, over what section of this range the response in linear. At the lower level is the detection limit. This has a precise definition according to the IUPAC convention. It is the concentration of analytes at which the extrapolated linear portion of the calibration graph intersects the baseline, a horizontal line corresponding to zero change in response for several decades of concentration change. With chemical sensor, the result usually shows the change in resistance lead to the sensing performance. The sensitivity (or sensor signal, sensor response), S is defined (Figure 1.13) as the several ratios depending on the types of a semiconductor, and the types of the analyte gases i.e. R_a/R_g [88−90], R_a-R_g/R_g [91,92], R_a-R_g/R_a [93], R_f-R_o/R_o [94], G/G_o [95], where R_a is the resistance in dry air, R_g is the resistance in test gas, R_f is the full-scale conductance when the sensor is in equilibrium with the gas, R_o is the baseline conductance when the sensor is in equilibrium with air, G is the conductivity in presence of gas, and G_o is the conductivity in air. In this research, the sensitivity is given in the following as the resistance ratio R_a/R_g for reducing gases e.g. C_2H_5OH, NH_3, SO_2, H_2, CO, and as R_g/R_a for oxidizing gases e.g. NO_2 [96] as shown in Equations 1.14 and 1.15 as follows:

$$S = \frac{R_a}{R_g} \quad \text{(for reducing gas)} \tag{1.14}$$

$$S = \frac{R_g}{R_a} \quad \text{(for oxidizing gas)} \tag{1.15}$$

1.6.3 Time factors [85, 87]

1.6.3.1 Response time [85, 87]

Many analytical devices require some “settling-down” time, i.e. time to allow the system to come to equilibrium, the response time. This is true to some extent with many chemical methods. For example, recent extensive studies with amperometric sensor showed that the most reproducible results were obtained after stirring the solution in contact with the electrode for ca. 30 s. However, with sensors of a chemical or biochemical nature this response time is greatly offset by the simplicity of the measurement and the minimal sample preparation time. Normally, the response times can vary from a few seconds to a few minutes. Up to 5 min may be acceptable, but if the time exceeds 10 min this may be too long. Normally, the response time, T_{res} is defined as the time required until 90 % of the response signal is reached [85, 91, 97, 98].

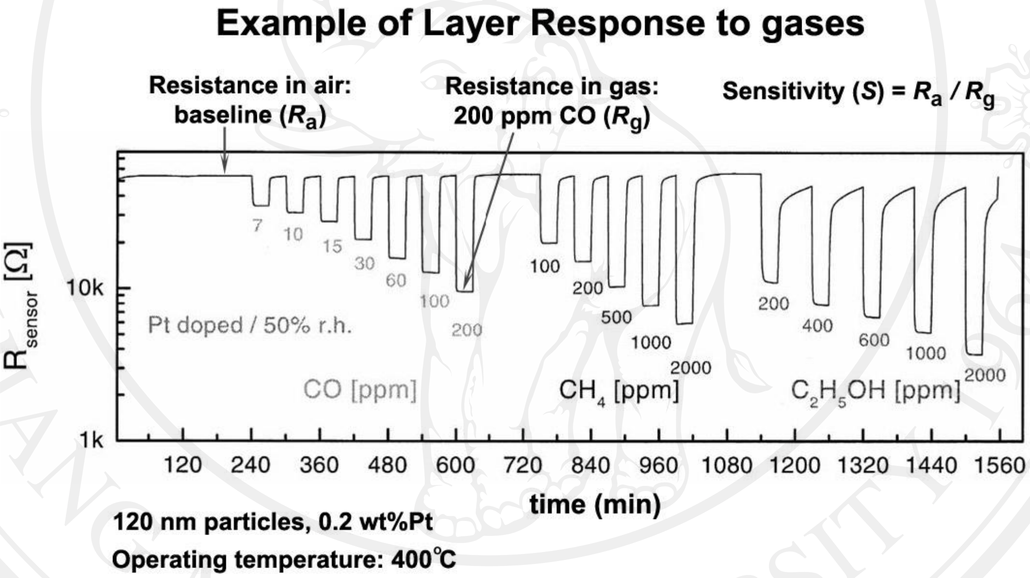

Figure 1.13 Change in resistance of several gases corresponded to the sensing performance in terms of sensitivity, response, and recovery times [99]

1.6.3.2 Recovery time [85, 87]

Very much related to the response time is the recovery time. The recovery time is the time that elapses before a sensor is ready to be used for another sample measurement. The resulting response time may be immediate or it may be that after one measurement the sensor system has to rest the resume its base equilibrium before it can be used with the next sample. In many publications, these times are combined and the result is given as the number of samples that can be analyzed per hour, which obviously is the main practical point at the end. In this research, the response and recovery times are important parameters for designing sensors for the desired application. The response/recovery times are defined as the time required for adsorption and desorption of oxygen on, or from the sensor surface to reach the saturation or to reduce the conductivity back to the baseline conductance. A good sensor is the one that shows a short response and recovery time. Normally, the recovery times, T_{rec} denotes the time needed until 90 % of the original baseline signal is recovered [85, 91, 97, 98]. The response and recovery time can be calculated using Equations 1.16 and 1.17 as follows:

$$T_{res} = \left[T_{R_O} - \left\{ \left(T_{R_O} - T_{R_g} \right) \right\} x \frac{90}{100} \right] - T_{R_O} \qquad (1.16)$$

$$T_{rec} = \left[T_{R_g} - \left\{ \left(T_{R_O} - T_{R_g} \right) \right\} x \frac{90}{100} \right] - T_{R_g} \qquad (1.17)$$

where $T_{\mathrm{Ro}}$is defined the as the time (s) at the baseline resistance in dry air (R_{a}) and T_{Rg} is denoted as the time (s) at the resistance in test gas (R_{g})**.**

1.7 Sensor experiment [100−110]

1.7.1 Semiconducting oxide sensors [100]

Gas sensors based on solid-state semiconductor materials offer considerable advantages in comparison to other gas sensing methods. Semiconductor sensors are inexpensive to produce, easy to miniaturize, rugged, reliable and can be designed to operate over a wide range of conditions including high temperature. Semiconductor sensors can be produced in array to allow sensing of multiple species simultaneously detected and with advances in sensitivity; detectivity limits which are approaching part-per-million (ppm) levels for some species.

1.7.1.1 Deposition-preparation of the sensitive layer [101−103]

The synthesis and deposition of the sensing layer is obviously the most crucial part in the preparation of gas sensors. Three main groups can be distinguished: powder/slurry deposition, chemical vapor deposition (CVD) and physical vapor deposition (PVD) [101, 102] (Table 1.4). The main difference between powder/slurry based films and CVD or PVD has traditionally been attributed to their different film thickness. While the former lead to sensitive layers of several microns of thickness (thick films), the layer thickness of the latter varies between 20 and 1000 nm. Beyond this classification, there is a fundamental difference in the microstructure of these thick and thin films. Thin films are usually very ‘compact’ (not porous), so the interaction with gas is limited to the external surface of the sensitive layer. On the other hand, gas can penetrate through most of thick films and so the interaction can occur throughout the whole layer. This has led to some authors argue that thick film must be more sensitive than thin films [102], since the change of conductivity is not limited to the outermost zone of the sensitive layer but to the whole layer.

Nevertheless, this classification must be carefully taken. For instance, it is well known that spin-coating techniques, which are actually using a slurry, are able to obtain ‘thin films’ in the sense of thickness (and the slurry can be obtained by a sol-gel process, for instance), being actually ‘thick films’ in terms of porosity [103]. As regards screen-printing, it must be understood that this technique is a two-step process: firstly the powder is obtained (by sol-gel, precipitation or any other method) and then a slurry based on this powder is screen printed. Regarding substrates, thick films have been typically deposited on alumina substrates provided with electrodes (usually interdigitated) and a heater. Thin films are of course deposited on flatter surface, i.e. silicon, what allows the use of micromachined gas sensors. However, the compatibility between powder technology and micromachined substrates have been also presented recently, what opens a new line of low power consumption gas sensors with thick sensitive films [102, 104−107].

Table 1.4 Typical deposition techniques used for the preparation of gas-sensitive materials based on semiconductors [108].

Powder/Slurry	***CVD***	***PVD***	
		Sputtering	***Evaporation***
Sol-gel	Thermal CVD	Sputtering	Molecular beam epit.
Precipitation	Plasma CVD	Reactive sputtering	Thermal evaporation
Screen-printing	Laser induced CVD	Cathode sputtering	Reactive evaporation
Dip coating	Electroless plating		Ion plating
Drop coating			Reactive ion plating
Pulverisation coating			Arc evaporation
Spin coating			Laser evaporation

1.7.1.2 Operation principles of the semiconducting gas sensor [109]

The principle of operation of semiconducting gas sensors is based on the change in conductance of the oxide on interaction with a gas and the change is usually proportional to the concentration of the gas. There are two types of semiconducting gas sensors; *n*-type (ZnO, SnO_2, WO_3) which respond to reducing gases and *p*-type (CoO, CuO) which respond to oxidizing gases. The *n*-type sensor operates as follows: oxygen in the air reacts with the surface of the sensor or at the grain boundaries of the oxide grains. This produces large resistance in these areas due to the lack of carriers and the resulting potential barriers produced between the grains inhibit the carrier mobility. However, if the sensor is introduced to a reducing gas like H_2, CH_4, CO, C_2H_5 or H_2S the resistance drops because the gas reacts with the oxygen and releases an electron. This lowers the potential barrier and allows the electrons to flow, thereby increasing the conductivity. P-type sensors respond to oxidizing gases like O_2, NO_2, and Cl_2 as these gases remove electrons and produce holes, i.e. producing charge carriers.

1.7.1.3 Mechanism for gas sensing in WO_3 sensors [100, 108]

WO_3 is an *n*-type semiconductor, where the sensor conductivity increase in the presence of a reducing gases, and decrease in the presence of an oxidizing gas. WO_3 sensor response is due to surface interactions between the WO_3 and the surrounding gases. The general steps involved in sensor response upon exposure to air and to a reducing gas, R, are shown in Figure 1.14. As shown in the figure 1.14, oxygen from the air is adsorbed onto the surface of the WO_3. Electrons from the surface region of the WO_3 are transferred to the adsorbed oxygen, leading to the formation of an electron-depleted region near the surface of the WO_3 particle. The electron depleted region, also called the space-charge layer, is an area of high resistance and the core region of the particle, where electron densities are high, is an area of relatively low resistance.

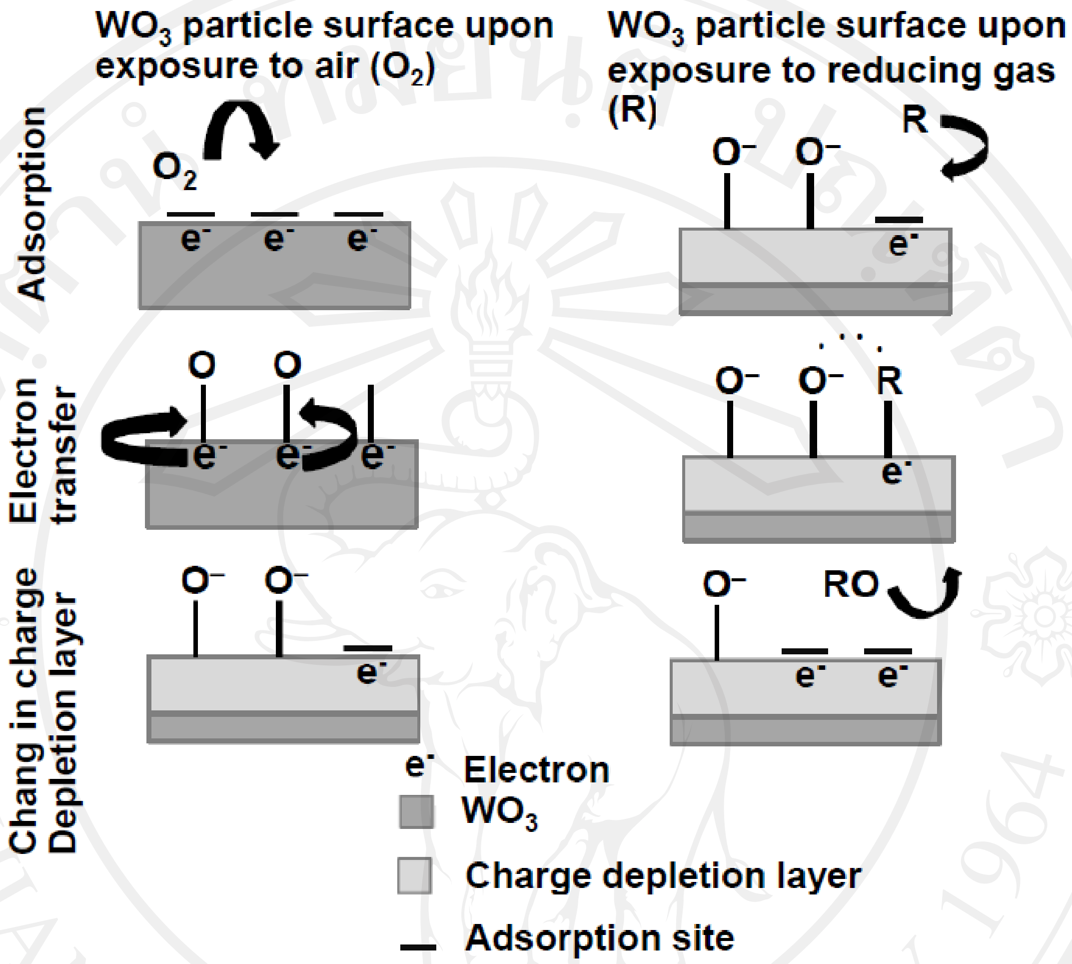

Figure 1.14 Schematics indicating the mechanisms leading to WO_3 sensor response to oxidizing and reducing gases [100].

The form of the adsorbed oxygen (either molecular or atomic) depends on the temperature of the sensor, where O_2^- species have been observed at lower temperatures (below 200°C) and O^- or O^{2-} species have been observed at higher temperature (above 200°C) [108]. The process can be expressed in the following reactions [110]:

$$O_2\text{ (gas)} \rightarrow O_2\text{ (absorbed)} \tag{1.18}$$

$$O_2\text{ (absorbed)} + e^- \rightarrow O_2^-\text{ (adsorbed)} \tag{1.19}$$

$$O_2^{-}\ \text{(adsorbed)} + e^{-} \rightarrow 2O^{-}\ \text{(adsorbed)} \tag{1.20}$$

$$O^{-}\ \text{(adsorbed)} + e^{-} \rightarrow O^{2-}\ \text{(adsorbed)} \tag{1.21}$$

When WO_3 surfaces are exposed to oxidizing gas such as NO_2, this gas react with the adsorbed O^{-} ions as well as adsorb directly on the surface of WO_3 surface. The oxidizing reactions between WO_3 and NO_2 gas follow the reaction paths [111]:

$$NO_2\,(g) + e^{-} \leftrightarrow NO_2^{-}\,(ads) \tag{1.22}$$

$$NO_2\,(g) + e^{-} \leftrightarrow NO(g) + O^{-}\,(ads) \tag{1.23}$$

And then the WO_3 surface is exposed to reducing gases, the gas reacts with the chemisorbed oxygen thereby releasing electrons back to the conduction band. The overall reducing reactions between NH_3, H_2S, CO, SO_2 CH_4, H_2, C_2H_2 and C_2H_5OH gases, and the chemisorbed oxygen species (O^{-} and O^{2-}) are given by [112–124]:

$$2NH_3 + 3O^{-}\,\text{(ads)} \rightarrow N_2 + 3H_2O + 3e^{-} \tag{1.24}$$

$$2NH_3 + 3O^{2-}\,\text{(ads)} \rightarrow N_2 + 3H_2O + 6e^{-} \tag{1.25}$$

$$H_2S + 3O^{-}\,\text{(ads)} \rightarrow H_2O + SO_2 + 3e^{-} \tag{1.26}$$

$$H_2S + 3O^{2-}\,\text{(ads)} \rightarrow H_2O + SO_2 + 6e^{-} \tag{1.27}$$

$$CO + O^{-}\,\text{(ads)} \rightarrow CO_2 + e^{-} \tag{1.28}$$

$$CO + O^{2-}\,\text{(ads)} \rightarrow CO_2 + 2e^{-} \tag{1.29}$$

$$SO_2 + O^{-}\,\text{(ads)} \rightarrow SO_3 + e^{-} \tag{1.30}$$

$$SO_2 + O^{2-}\,\text{(ads)} \rightarrow SO_3 + 2e^{-} \tag{1.31}$$

$$CH_4 + 4O^{-}\,\text{(ads)} \rightarrow 2H_2O + CO_2 + 4e^{-} \tag{1.32}$$

$$CH_4 + 4O^{2-}\,\text{(ads)} \rightarrow 2H_2O + CO_2 + 8e^{-} \tag{1.33}$$

$$H_2 + O^{-}\,\text{(ads)} \rightarrow H_2O + e^{-} \tag{1.34}$$

$$H_2 + O^{2-}\,\text{(ads)} \rightarrow H_2O + 2e^{-} \tag{1.35}$$

$$C_2H_2 + O^- \text{ (ads)} \rightarrow H_2O + 2C + e^- \qquad (1.36)$$

$$C_2H_5OH \text{ (gas)} + O^- \Leftrightarrow CH_3CHO + H_2O + e^- \qquad (1.37)$$

$$C_2H_5OH \text{ (gas)} \Leftrightarrow H + C_2H_5O \text{ (surface)} \qquad (1.38)$$

$$C_2H_5O \rightarrow H + CH_3CHO \qquad (1.39)$$

$$CH_3CHO + O \text{ (bulk)} \rightarrow CH_3COOH + O \text{ (vacancies)} \qquad (1.40)$$

Crystallite size effects on sensor performance are generally explained in terms of the relative values of the characteristic dimensions of the connection between adjacent particles (the neck width) and of the thickness of the space charge layer. The thickness of the space charge layer is typically indicated by the Debye length (L_D) of the electrons in WO_3. Figure 1.15 shows the various regimes that are of interest in WO_3 sensors based on the relative values of the neck width and the Debye length. The intergranular contacts between WO_3 particles can be classified into three categories: open neck, closed neck and Schottky contact-type connections. The dramatic dependence of sensor sensitivity on WO_3 particle size can be understood by considering the size regimes outlined in Figure 1.15. As the crystallite dimension decreases relative to the Debye length (L_D) of the electrons in WO_3, the sensor conductance becomes dominated by the high resistance of the interparticle neck. Under these conditions, the sensor sensitivity is a very strong function of the size of the necks between the particles [100].

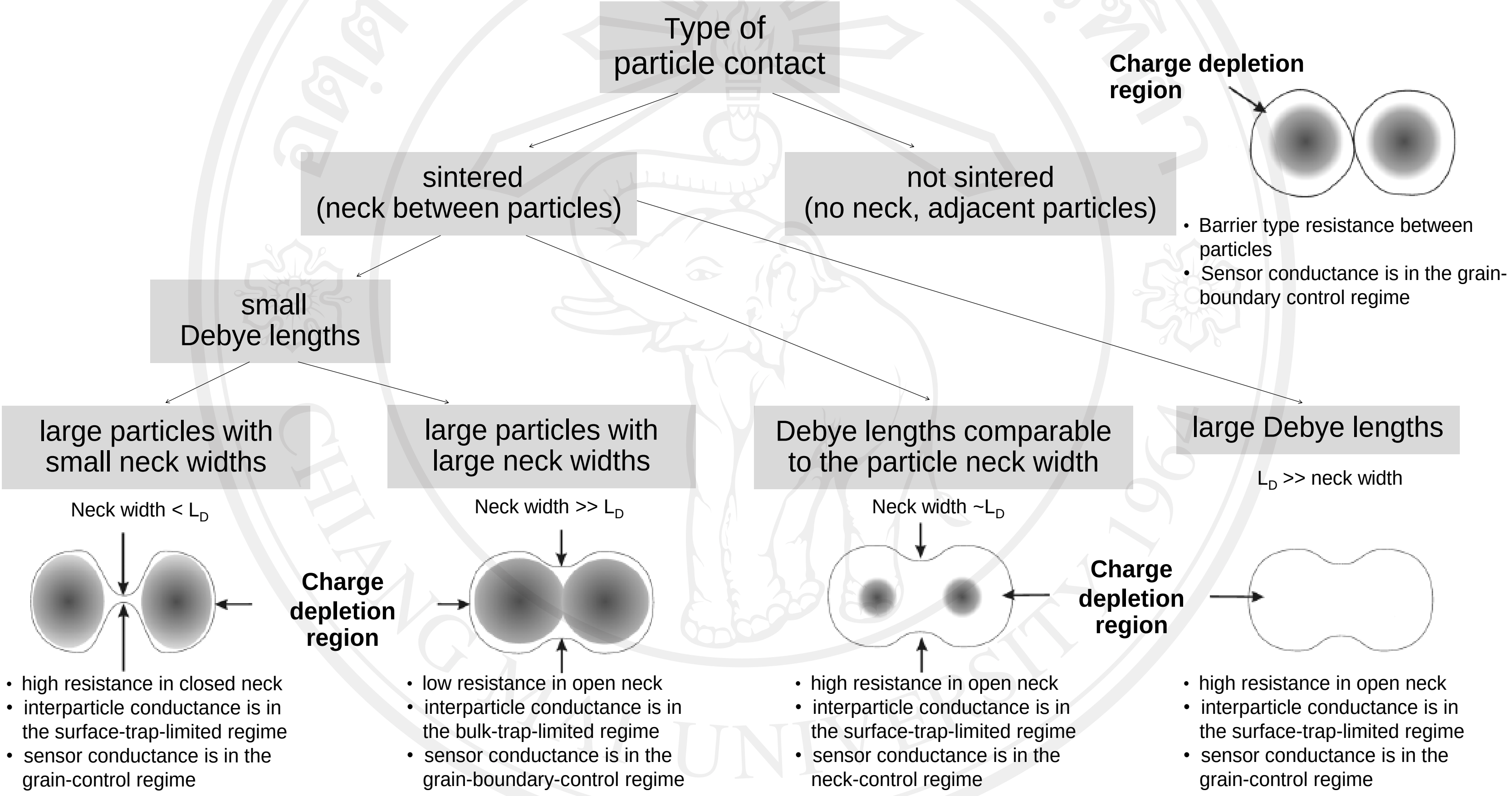

Figure 1.15 Schematics indicating the conductance mechanisms important in the various WO_3 crystallite size regimes, relative to the WO_3 electron Debye length, L_D [100]

1.7.1.4 Catalytic additives on semiconducting oxide sensors [108]

The addition of an appropriate amount of metal additives has been shown to improve the detection of various kinds of gases via the enhancement of the sensor response and a decrease of the temperature of maximum sensor response. A decrease in response time and better selectivity are also claimed to be achievable by using these additives.

The use of additives on semiconducting oxides is evidently related to the use of supported metal/semiconducting oxide in catalysis. In this field, the main target is to enhance the reaction rate of the gases. On the other hand, in the field of semiconducting oxide sensors, this higher rate of reaction must be translated into an electrical signal; otherwise no advantage for gas sensing is taken from catalyzing the reaction.

It is accepted that metal additives can lead to two different sensitization mechanisms: chemical sensitization and electronic sensitization [125]. In the first case, the promoting effect is due to the ability of noble metal to activate inflammable gases by enhancing their spill-over, so that they react with oxygen adsorbates more easily. Besides, the supply of oxygen can be enhanced by the presence of these catalytic additives, at the surface of which oxygen molecules from the gas phase can be easily dissociated and oxygen atoms migrate through spill-over effect to the surface of the semiconducting oxide. In this way, the additive exerts a sort of remote control on the catalytic and sensing properties of the semiconducting oxide.

On the other hand, the electronic sensitization is associated with oxidized metal additives. The addition of fine particles of some metals to n-type metal oxides usually results in a rise of the base resistance in air. There is a decrease in the electron concentration in the oxide surface layer, which corresponds to an increase of the space-charge depth as a result of the electron transfer from the metal oxide to the metal loaded onto its surface. When the metal surface is covered with oxygen adsorbates at elevated temperatures in air (i.e. the metal is oxidized), the oxygen adsorbates extract electrons from this metal, which in turn extracts electrons from the metal oxide, leading to a further increase in the space-charge depth. Consumption of oxygen adsorbates on the metal, in addition to those on the semiconducting oxide surface, by reaction with flammable gases, causes the enhanced sensitivity. In this case, therefore, the promoting effect arises mainly from the change in the oxidation state of the loaded material.

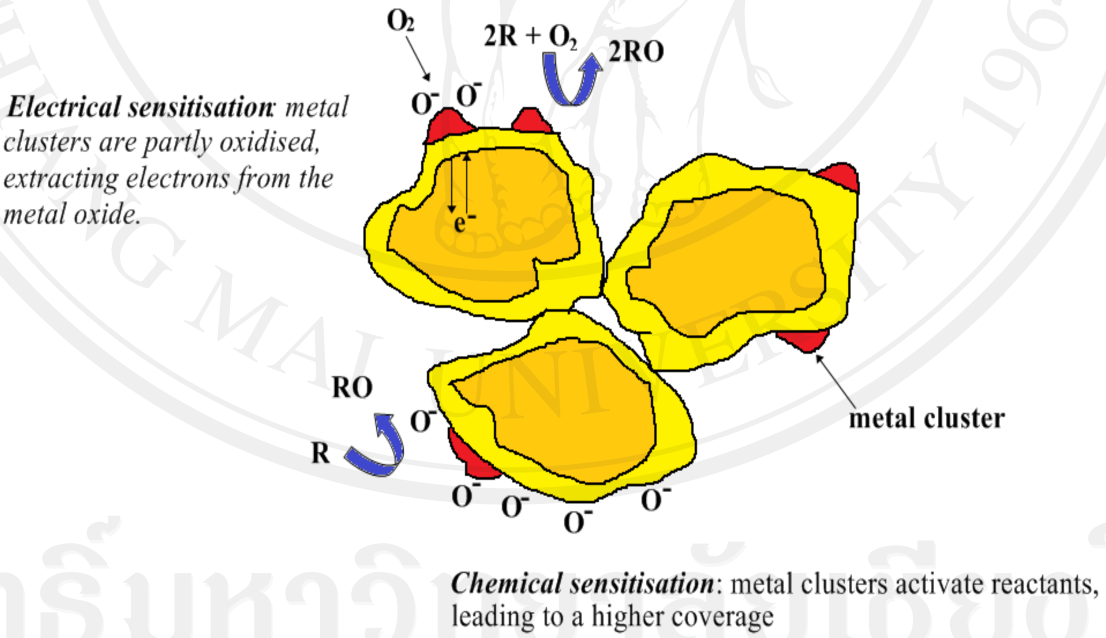

Figure 1.16 Catalytic additives on semiconducting oxide sensors. Top: Electrical sensitization - oxidation state of metallic clusters depend on ambient gases. Bottom: Chemical sensitization – metallic clusters promote the activation of gaseous specie [108].

1.8 Literature reviews [13, 24−25, 28, 30, 126−130]

In 1995, tungsten oxide (WO_3) sputtered thin films for NO_x monitoring were reported by Sberveglieri *et al*. [126]. WO_3 thin films were deposited by reactive sputtering (r.f. sputtering) onto a 3 mm x 3 mm alumina substrate. The characterization either of their structural properties by mean of X-ray diffraction (XRD) measurements or of the film morphology with the Atomic force microscopy (AFM) and the electrical response of the films towards toxic and pollutant gases. XRD patterns showed triclinic phase of WO_3.This phase was stable from about -40^{o}C to about +17^{o}C, but it was possible that film growth in conditions out of equilibrium could stabilize it. An AFM micrograph of the WO_3 surface indicated that the film surface was wrinkled with the presence of many agglomerates with an average size of about 1μm. For the sensor tested, WO_3 thin films showed a good sensitivity towards low NO_x concentrations (1−10 ppm) in the temperature interval of 200−500^{o}C and they were also sensitive to 10 ppm NH_3. These films were also rather insensitive to other reducing gases like 1000 ppm of CH_4, 100 ppm of CO and 10 ppm of SO_2 in the range 300−500^{o}C (the sensitivity is lower than 0.5 in all cases).

In 1998, WO_3-base gas sensor devices was fabricated by reactive rf sputtering on glass substrates as reported by Penza *et al*. [13]. Palladium (Pd), platinum (Pt), gold (Au) noble metals (100−600^{o}C) were evaporated as activator layers onto WO_3 thin films and Al layers (1500Å) were sputtered on top of them as upper electrodes for sensor output. These sensors are very promising for NO_2 and NO gas detection at low temperatures (150−250^{o}C). Best performances was obtained at 150, 200, 250^{o}C for WO_3:Pt, WO_3:Pd and WO_3:Au, undoped WO_3, respectively, with 600Å thick catalyst. The resistance of the thin-film gas sensor increased reversibly in the presence of low concentrations of NO (0−440 ppm) and NO_2 (0−10 ppm) gases in air. The activator layers have promotional effect on the speed of response to NO_x at low temperatures and on selectivity enhanced with respect to other reducing gases (CO, CH_4, H_2, SO_2, H_2S, NH_3).

In 2005, the gas sensing performance of Pt and Au catalysts activated WO_3 thin films were investigated by Ippolito *et al*. [127]. The WO_3 thin films were deposited onto alumina transducers with platinum inter-digital electrodes using a R.F. magnetron sputtering. Maximum sensitivity for the Pt-WO_3, Au-WO_3 and bare WO_3 sensor were obtained at operating temperatures of 70, 262 and 180^{o}C, respectively. The response of the sensors with Pt and Au activator layers showed that they are approximately 161 and 40 times more sensitive than the bare WO_3 film, respectively. The response of the Au-WO_3 sensor was found to be more stable than that of the Pt-WO_3, although it required a significantly higher operating temperature.

In 2006, the controlled synthesis of two novel h-WO_3 hierarchical structures made of nanorods/nanowires has been successfully realized in a large scale via a simple hydrothermal method was reported by Gu *et al*. [128]. It was demonstrated that the morphology of the final products was significantly influenced by adding different sulfates. The urchinlike and ribbonlike structures of WO_3 can be selectively prepared by adding Rb_2SO_4 and K_2SO_4, respectively. The morphology evolvement and the growth mechanism were studied carefully. The sulfate-induced oriented attachment growth mechanism has been proposed for the possible formation mechanism of the ribbonlike sample. For urchinlike products, two growing stages were believed to be involved in the growth process.

In 2007, ethanol vapor sensing properties of WO_3 thick films was presented by Khadayate *et al*. [129]. WO_3 thick films were prepared by using screen printing method. These thick films were characterized by using XRD and SEM coupled with energy-dispersive X-rays (EDX). The ethanol vapor sensing properties were investigated at different operating temperatures and gas concentrations. The WO_3 thick films exhibit excellent ethanol vapor sensing properties with maximum sensitivity, ~1424.6% at 400^{o}C, with fast response and recovery time. Furthermore, it was shown that the screen printed WO_3 thick films can be reliably used to monitor the concentration of ethanol vapor over the range 25−75 ppm. The response and recovery characteristics of WO_3 thick films were almost reproducible and quick.

In 2007, NH_3 selective gas sensor based on tungsten oxide nanopowder films were successfully synthesized using acid precipitation method was reported by Wang *et al*. [130]. The product has a new hexagonal structured metastable phase rather than common stable phases of tungsten oxides, such as monoclinic etc. The synthesized h-WO_3 sensor has a very high sensitivity to NH_3 gas, up to 88%, 92%, and 96% responding to 50 ppm, 100 ppm, and 200 ppm of NH_3, respectively, which is much higher than that of γ-WO_3 sensor which has similar morphology and sizes. It is believed that it is the more open structure of h-WO_3 that improves its sensitivity compared to other stable phases.

In 2008, ε-WO_3 nanoparticles was produced successfully by flame spray pyrolysis (FSP) by Wang *et al*. [24]. Cr doping was able to stabilize this eccentric structure during heat treatment. The structures of pure and doped WO_3 particles were characterized using Raman spectroscopy. It was found that all as-synthesized products contain a fairly high percentage of ε-WO_3. The ε-WO_3 content increased as the Cr concentration increased. After heat treatment, pure WO_3 experienced a significant phase transition, in which the ε-WO_3 phase mostly transformed to γ phase. A sensor with 10 at.% Cr-doped WO_3 nanoparticles was prepared to investigate its response to acetone vapor. The temperature was set to 400°C, and the concentrations of the gases were 0.2−1 ppm. The 10 at.% Cr-doped WO_3 nanoparticle-based sensor was capable of real-time, fast-response, stable, and highly sensitive detection of acetone gas. As a result, flame-made nanostructural sensor can be good candidate for diabetes diagnosis based on human breath analysis.

In 2008, WO_3 was grown by direct thermal evaporation of metal tungsten foils in an oxygen atmosphere by Siciliano *et al*. [25]. The samples were characterized by SEM, EDX and Raman spectroscopy. The synthesized products consisted of crystalline aggregates having a mean size of about 0.8μm. Raman spectroscopy evidenced typical vibrational peaks of the monoclinic WO_3 phase. The gas sensing properties of the samples were studied for the detection of NO_2, NO and NH_3 gases. In the case of NO and NO_2 gases, the resistance of the films increased and attained a saturation value. The resistance always returned to its initial value after the test gases had been shut off. The response transient of the sensor to NH_3 gas, however, was a mirror image of those to NO and NO_2 gases. In an *n*-type semiconductor, such as WO_3, the reducing gas NH_3 liberates free electrons, and decreases the resistivity of the films, whereas the oxidizing gases NO and NO_2 take up free electrons, leading to an increase in resistivity of the films. It was found that WO_3 samples were suitable for NO_2 gas detection at about 250°C. The response towards a wide range of gas concentrations was found to follow a power-law relationship. The response to NO_2 was large compared to that to NO in the investigated temperature range. The samples were relatively insensitive to NH_3 gas. The electrical properties were reproducible during the long-term stability test.

In 2009, tungsten trioxide powder with the novel morphology was prepared via the hydrothermal method with oxalic acid as the organic inducer as reported by Yi *et al*. [28]. The structure and shape of which were detected by XRD, SEM and BET. Furthermore, photochromic properties of the as-prepared powder samples were tested by an ultraviolet-visible spectrophotometer combined with a color difference meter. The corresponding results indicated that the induced product was still hexagonal WO_3, made up of regularly spindle particles with 200−300 nm in length and 30−50 nm in width. The ratio of the length and width was from 4 to 10. Moreover, the special morphology improved its absorptive capacity to the excitation light source, resulting in its high photochromic properties.

In 2009, WO_3 nanorods were synthesized by a facile hydrothermal process with $Na_2WO_42H_2O$ as the tungsten source and NaCl as the capping agent was reported by Wang *et al*. [131]. Systematic investigations of the influence of precursor pH and the amount of capping agent on the morphologies of the products have been carried out. It was found that uniform crystalline WO_3 nanorods can by synthesized at pH 2.0 with suitable NaCl content. A transparent thin film was successfully prepared by coating the as-synthesized WO_3 nanorods onto the surface of ITO-coated glass. The film showed fast electrochromic switching response, comparable constrast and coloration efficiency, and much higher charge density (114.5 mC cm^{-2} mg^{-1}) than conventional amorphous WO_3 films in 0.5 mol/L H_2SO_4 electrolyte. The fast switching response and high H^+ insertion ability of the as-prepared electrochromic film were attributed to the large active specific surface area of the as-synthesized WO_3 nanorods and the application of acidic electrolyte (H_2SO_4) containing smaller inserted ions (H^+) than Li^+ ions in lithium-based electrolytes.

In 2010, a novel sensor material of WO_3 supported Pt clusters hybrid material was synthesized by Zhang *et al*. [88]. The as-prepared WO_3 supported Pt cluster composites were characterized by means of XRD, TEM and XPS. TEM images showed that the Pt clusters with a size of ca. 2 nm were uniformly dispersed on the surface of WO_3 support. Gas sensing tests revealed that the Pt/WO_3 hybrid material with a Pt content of 2.36 wt.% exhibits the best response towards ethanol detection at an operating temperature of 140^oC. The sensor also possesses fast response and recovery characteristics, good selectivity and stability. The enhanced sensor performance was interpreted in terms of the proper content, uniform dispersion and small size of Pt clusters, which probably have a strong spillover effect and can serve as active sites for sensing reactions and excellent channel for electron transfer in the process of sensing reactions. The electronic interaction between Pt clusters and WO_3 support is also believed to contribute to the improved sensor performance.

In 2010, two kinds of tungsten oxide (WO_3) square nanoplates have been prepared by a simple hydrothermal method using L(+)-tartaric acid or citric acid as assistant agents as reported by Su *et al*. [30]. XRD, SEM and TEM images of the products illustrated that WO_3 square nanostructures prepared in the presence of L(+)-tartaric acid had a hexagonal phase, length of ~200 nm and thickness of ~100 nm, while WO_3 nanostructures synthesized in the presence of citric acid had an orthorhombic phase, length of ~500 nm and thickness of ~100 nm. Selected area electron diffraction (SAED) suggested that both of the as-prepared WO_3 square nanoplates were single crystalline.

Table 1.5 shows the summary of size and morphology of unloaded WO_3 and Pt-loaded WO_3 nanoparticles prepared by several methods.

Table 1.5 A summary of size and morphology of unloaded WO_3 and Pt-loaded WO_3 nanoparticles prepared by several methods.

Method	**Size**	**Morphology**	**Reference**
Hydrothermal method	Diameter: ~100 nm Length: 1−2 μm	Nanowires (h-WO_3)	[20]
Precipitation method	8 nm (grain size)	Nanocrystalline	[26]
Hydrothermal method	34 nm (grain size) Diameter: 200−300 nm Length: 30−50 nm	Nanometer (h-WO_3)	[28]
Hydrothermal method	Length: ~200 nm Thickness: ~100 nm Length: ~500 nm Thickness: ~100 nm	Square nanostructures (h-WO_3) Nanostructures (ortho-WO_3)	[30]
Solvothermal synthesis	~2 μm in size and 250 nm in thickness (h-WO_3) 150 nm (m-WO_3)	Hexagonal platelets (h-WO_3) Square nanosheets (m-WO_3)	[31]
Hydrothermal method	Diameter: 10 nm Length: ~ μm	Nanowires	[132]
Acid precipitation method	190 ± 15 nm wide and 50 ± 15 nm thick 30 nm (average size)	Nanoplates	[133]
Aged-hydrothermal method	Diameter: 20−70 nm Length: 30−200 nm	Nanostructures	[134]

Table 1.5 (Cont.) A summary of size and morphology of unloaded WO_3 and Pt-loaded WO_3 nanoparticles prepared by several methods.

Method	**Size**	**Morphology**	**Reference**
Hydrothermal method	Diameter: 50−70 nm Length: up to 5μm	Nanorods	[135]
Precipitation method	30−45 nm (crystallite size) 0.1−3.0 μm	No report	[136]
Acid precipitation method	Nanoparticles: 10−50 in diameter Nanorods: 30−100 nm in diameter and 100−300 nm in length	Hexagonal (h-WO_3)	[137]

Table 1.6 shows the summary on the gas sensing properties of differently prepared unloaded WO_3 and Pt-loaded WO_3 towards reducing gas.

Table 1.6 A summary on the gas sensing properties of differently prepared unloaded WO_3 and Pt-loaded WO_3 towards reducing gas.

Sensing materials	Method	Gas Concentration	Response	Reference
Unloaded WO_3	Reactive rf sputtering (sensors)	H_2 ; 500 ppm	~ 0.01 at $250^{o}C$	[13]
Pt-loaded WO_3			~ 0.02 at $150^{o}C$	
Unloaded WO_3		CO; 1000 ppm	~ 0.05 at $250^{o}C$	
Pt-loaded WO_3			~ 0.05 at $150^{o}C$	
Unloaded WO_3		SO_2 ; 10 ppm	~ 0.4 at $250^{o}C$	
Pt-loaded WO_3			~ 0.3 at $150^{o}C$	
Unloaded WO_3		H_2S ; 10 ppm	~ 0.85 at $250^{o}C$	
Pt-loaded WO_3			~ 1.1 at $150^{o}C$	
Unloaded WO_3		CH_4 ; 7000 ppm	~ 1.05 at $250^{o}C$	
Pt-loaded WO_3			~ 1.19 at $150^{o}C$	
Pt-loaded WO_3	sputtering (sensors)	H_2 ; 100 ppm	~ 7.4 at $220^{o}C$	[14]
		CO; 100 ppm	~ 2.3 at $220^{o}C$	
		H_2S ; 50 ppm	~ 1250 at $220^{o}C$	
		CH_4 ; 1000 ppm	~ 0.05 at $220^{o}C$	

Table 1.6 (Cont.) A summary on the gas sensing properties of differently prepared unloaded WO_3 and Pt-loaded WO_3 towards reducing gas.

Sensing materials	**Method**	**Gas Concentration**	**Response**	**Reference**
Unloaded WO_3	Precipitation	C_2H_4 ; 10 ppm	~4.5 at 300°C	[23]
2.36 wt.%Pt/WO_3	Spin-coating (sensors)	C_2H_5OH ; 100 ppm	~ 87.1 at 140°C	[88]
Unloaded WO_3	Reactive magnetron sputtering (sensors)	H_2 ; 1000 ppm	~ 13.6 at 300°C	[93]
Unloaded WO_3	Reactive sputtering (sensors)	CO ; 100 ppm SO_2 ; 10 ppm	< 0.5 at 300−500°C < 0.5 at 300−500°C	[126]
Unloaded WO_3 Pt-loaded WO_3	R.F. magnetron sputtering (sensors)	H_2 ; 1 vol.%	~ 9 at 150°C ~1600 at 70°C, ~ 200 at 150°C	[127]
Unloaded WO_3	Screen-printing (sensors)	C_2H_5OH ; 50 ppm	~1424.6 at 400°C	[129]
0.4 wt.%Pt/WO_3	Screen-printing (sensors)	CO ; 800 ppm C_2H_5OH ; 160 ppm	~1.5 at 450°C ~2 at 450°C	[138]
0.5 at.%Pt/WO_3	Radio frequency sputtering	H_2 ; 200 ppm	~26 at 95°C	[139]

Table 1.7 A summary on the gas sensing properties of differently prepared unloaded WO_3 and Pt-loaded WO_3 towards oxidizing gas.

Table 1.7 A summary on the gas sensing properties of differently prepared unloaded WO_3 and Pt-loaded WO_3 towards oxidizing gas.

Sensing materials	**Method**	**Gas Concentration**	**Response**	**Reference**
Unloaded WO_3 Pt-loaded WO_3	Reactive rf sputtering (sensors)	NO_2 ; 10 ppm	~ 2 at 250^{o}C ~ 3.45 at150^{o}C	[13]
Unloaded WO_3	FSP	NO_2 ; 1 ppm	<1.1 at 300^{o}C	[24]
Unloaded WO_3	Thermal oxidation of tungsten	NO_2 ; 100 ppm	~32 at 240^{o}C	[25]
Unloaded WO_3	Reactive magnetron sputtering (sensors)	NO_2 ; 1 ppm	~ 460 at 200^{o}C	[93]
Unloaded WO_3	Electrostatic spray deposition	NO_2 ; 1 ppm	~8 at 200^{o}C	[117]
0.4 wt.%Pt/WO_3	Screen-printing (sensors)	NO_2 ; 400 ppm	~4 at 450^{o}C	[138]
Unloaded WO_3	Photolithography and bulk micro machining technique	NO_2 ; 30 ppm	~ 9 at 300^{o}C	[140]

Table 1.7 (Cont.) A summary on the gas sensing properties of differently prepared unloaded WO_3 and Pt-loaded WO_3 towards oxidizing gas.

Sensing materials	**Method**	**Gas Concentration**	**Response**	**Reference**
Unloaded WO_3	Sol-gel dip-coating on alumina substate (sensors)	NO_2 ; 10 ppm	~ 82 at 200°C	[141]
Unloaded WO_3	Reactive magnetron sputtering (sensors)	NO_2 ; 10 ppm	~58 at 150°C	[142]
Unloaded WO_3 Pt-loaded WO_3	Reactive rf sputtering	NO_2 ; 10 ppm	1.33 at 260°C 11.73 at 260°C	[143]
Unloaded WO_3	Hydrothermal	NO_2 ; 20 ppm	525 at 350°C	[144]
Unloaded WO_3	Atomspheric plasma spraying	NO_2 ; 450 ppb	77 at 130°C	[145]

1.9 Objective of the study

1.9.1 To synthesize of unloaded WO_3 and Pt-loaded WO_3 nanoparticles by FSP and other wet chemical methods

1.9.2 To characterize the of unloaded WO_3 and Pt-loaded WO_3 nanoparticles

1.9.3 To study the gas sensing properties of unloaded WO_3 and Pt-loaded WO_3 nanoparticles synthesized by FSP and other wet chemical methods

1.9.4 To study the morphology of nanoparticles and sensing films on their gas sensing properties

1.10 Usefulness of the Research (Theory and/or Applied)

1.10.1 The high purity and homogeneity powders produced by FSP in a single step will be obtained.

1.10.2 Knowledge of FSP and other wet chemical methods; preparation and characterization and properties of unloaded WO_3 and Pt/WO_3 nanoparticles will be obtained.

1.10.3 Knowledge of WO_3 and Pt/WO_3 nanoparticles for used as gas sensors will be obtained.

1.11 Research plan, methodology and scope

1.11.1 To review literature

1.11.2 To synthesize unloaded WO_3 and Pt-loaded WO_3 nanoparticles by FSP and the hydrothermal method

1.11.3 To characterization the particle properties facilitated by X-ray Diffraction (XRD), Scanning Electron Microscopy (SEM), Transmission Electron Microscopy (TEM), Energy Dispersive X-ray Spectroscopy (EDS) and Brunauer Emmett Teller (BET)

1.11.4 To test the gas sensing properties of unloaded WO_3 and Pt/WO_3 nanoparticles synthesized by FSP and the hydrothermal method

1.11.5 Discussion and conclusions